



# A microstructural study of fault rocks from the SAFOD: Implications for the deformation mechanisms and strength of the creeping segment of the San Andreas Fault

Jafar Hadizadeh<sup>a,\*</sup>, Silvia Mitterpergher<sup>b,c</sup>, Jean-Pierre Gratier<sup>c</sup>, Francois Renard<sup>c,d</sup>, Giulio Di Toro<sup>b,e</sup>, Julie Richard<sup>c</sup>, Hassan A. Babaie<sup>f</sup>

<sup>a</sup> 212 Lutz Hall, Department of Geography & Geosciences, University of Louisville, Louisville KY 40292, USA

<sup>b</sup> University of Padova, Padova, Italy

<sup>c</sup> ISTerre, University Joseph Fourier & CNRS, BP 53, 3804 Grenoble, France

<sup>d</sup> PGP, University of Oslo, Oslo, Norway

<sup>e</sup> Istituto Nazionale di Geofisica e Vulcanologia, Rome, Italy

<sup>f</sup> Geosciences, Georgia State University, Atlanta, GA, USA

## ARTICLE INFO

### Article history:

Received 13 June 2011

Received in revised form

23 April 2012

Accepted 24 April 2012

Available online 7 May 2012

### Keywords:

San Andreas Fault

SAFOD

Foliated gouge

Shear localization

Cataclasis

Pressure solution

## ABSTRACT

The San Andreas Fault zone in central California accommodates tectonic strain by stable slip and microseismic activity. We study microstructural controls of strength and deformation in the fault using core samples provided by the San Andreas Fault Observatory at Depth (SAFOD) including gouge corresponding to presently active shearing intervals in the main borehole. The methods of study include high-resolution optical and electron microscopy, X-ray fluorescence mapping, X-ray powder diffraction, energy dispersive X-ray spectroscopy, white light interferometry, and image processing.

The fault zone at the SAFOD site consists of a strongly deformed and foliated core zone that includes 2–3 m thick active shear zones, surrounded by less deformed rocks. Results suggest deformation and foliation of the core zone outside the active shear zones by alternating cataclasis and pressure solution mechanisms. The active shear zones, considered zones of large-scale shear localization, appear to be associated with an abundance of weak phases including smectite clays, serpentinite alteration products, and amorphous material. We suggest that deformation along the active shear zones is by a granular-type flow mechanism that involves frictional sliding of microlithons along phyllosilicate-rich Riedel shear surfaces as well as stress-driven diffusive mass transfer. The microstructural data may be interpreted to suggest that deformation in the active shear zones is strongly displacement-weakening. The fault creeps because the velocity strengthening weak gouge in the active shear zones is being sheared without strong restrengthening mechanisms such as cementation or fracture sealing. Possible mechanisms for the observed microseismicity in the creeping segment of the SAF include local high fluid pressure build-ups, hard asperity development by fracture-and-seal cycles, and stress build-up due to slip zone undulations.

© 2012 Elsevier Ltd. All rights reserved.

## 1. Introduction

The orientation of horizontal principal stresses and data from heat flow measurements require the San Andreas Fault (SAF) in central California to deform at a low resolved shear stress (Lachenbruch and Sass, 1992; Rice, 1992; Bird and Kong, 1994; Zoback, 2000; Townsend and Zoback, 2000; Hickman and Zoback,

2004; Chéry et al., 2004; Boness and Zoback, 2006). For the creeping segment of the SAF, mechanisms such as fluid overpressure and presence of intrinsically weak fault rocks have been invoked to support the weak fault model (e.g. Byerlee, 1993; Rice, 1992; Faulkner and Rutter, 2001; Lockner et al., 2011; Carpenter et al., 2011). Hydrological modeling of the SAF by Fulton and Saffer (2009), Fulton et al. (2009), and the results of Faulkner and Rutter (2001) by implication, ruled out fluid overpressure weakening by metamorphic dehydration, but did not rule out the possibility of fluid overpressure due to dehydration of mantle-derived serpentinites.

\* Corresponding author. Tel.: +1 502 852 2691.

E-mail addresses: [j0hadi01@louisville.edu](mailto:j0hadi01@louisville.edu), [hadizadeh@louisville.edu](mailto:hadizadeh@louisville.edu) (J. Hadizadeh).

The central California segment of the SAF exhibits creep that diminishes from ~28 mm/year, in the central region of the segment, to ~20 mm/year at the San Andreas Fault Observatory at Depth (SAFOD) site near Parkfield. The creep rate diminishes almost to zero at the southeast end of the segment where transition to a locked section of the SAF occurs near Fort Tejon (Titus et al., 2006). In addition to creep, the segment shows repeating  $M < 3$  earthquakes with an average recurrence time of ~3 years (Nadeau et al., 2004) on seismic patches with estimated 15–20 m radial dimensions (Nadeau and Johnson, 1998; Dreger et al., 2007). Seismic inversion studies near the observatory site show that the patches occur in roughly strike-parallel clusters that make up 1% or less of the total fault surface area (Nadeau and Johnson, 1998; Rubin et al., 1999; Waldhauser et al., 2004; Dreger et al., 2007; Chen and Lapusta, 2009). While the weak SAF is estimated to have coefficient of friction  $\mu < 0.2$ , the seismic asperity patches are expected to have  $\mu > 0.2$ , suggesting that the contrasting frictional strengths could serve as a source of mechanical instability (Townend and Zoback, 2004; Chéry et al., 2004; d'Alessio et al., 2006; Dreger et al., 2007; Imanishi and Ellsworth, 2006; McGarr et al., 2010). Nadeau et al. (1995) reported that locations of dominant repeating events appear to migrate cyclically within the clusters over several years. Establishment of the SAFOD is the latest effort to shed light on the strength model controversy and understand the nature of the creep and seismic activity in the SAF via direct observations (Fig. 1a). The discovery in 2005 of steel casing deformation within the SAFOD Main Hole revealed two distinct intervals of active shearing. The intervals (Fig. 1b) were subsequently named by Zoback et al. (2011) the Southwestern Deforming Zone (SDZ) and Central Deforming Zones (CDZ). The direct evidence of active shearing within the SAF core zone has made the microstructural features associated with the SDZ and CDZ more significant because majority of microstructural studies on fault rocks to date are from exhumed fault zones.

Zoback et al. (2011) outlined major findings of the SAFOD as: 1. Major fault strands of the SAF encountered in the drill hole consist of strongly foliated gouge, 2. The SAF acts as a barrier to fluid flow, 3. The maximum horizontal principal stress is at high angles to the SAF to within 100 m of the fault zone, 4. There are no temperature anomalies and no evidence of higher-than-hydrostatic fluid pressures in the SAFOD borehole. Recent investigations based on the SAFOD core and cuttings samples explain the fault's apparent absolute weakness mainly in terms of frictional weakness of the fault rock constituents. Solum and van der Pluijm (2004) and Solum et al. (2006, 2007) studied the authigenesis and distribution of phyllosilicate assemblages in the SAFOD cores and cuttings. These results showed concentrations of chlorite, illite, and illite-smectite along several identifiable strands of the SAF while smectite mineral saponite and serpentine mineral lizardite were found in samples from the active shear zones. Moore and Rymer (2007) suggested that their discovery of talc coating on serpentinite particles is a possible explanation for the weak fault model. Schleicher et al. (2008), however, found little or no talc associated with serpentinites in the fault gouge. Janssen et al. (2010) reported amorphous material in the foliated gouge samples close to the active shear zones. Holdsworth et al. (2011) concluded that the presence of low-friction Mg-rich smectites is a viable explanation for the creep behavior (velocity strengthening) and the absolute weakness, but suggested that the material weakness model may hold true only down to 5–6 km depths in this segment of the SAF. The latter conclusion was reached because Mg-rich smectites tend to breakdown into frictionally stronger Mg-rich chlorites at  $T > 150$  °C (Inoue and Utada, 1991). Wenk et al. (2010) determined that phyllosilicates in the SAFOD gouge had a much

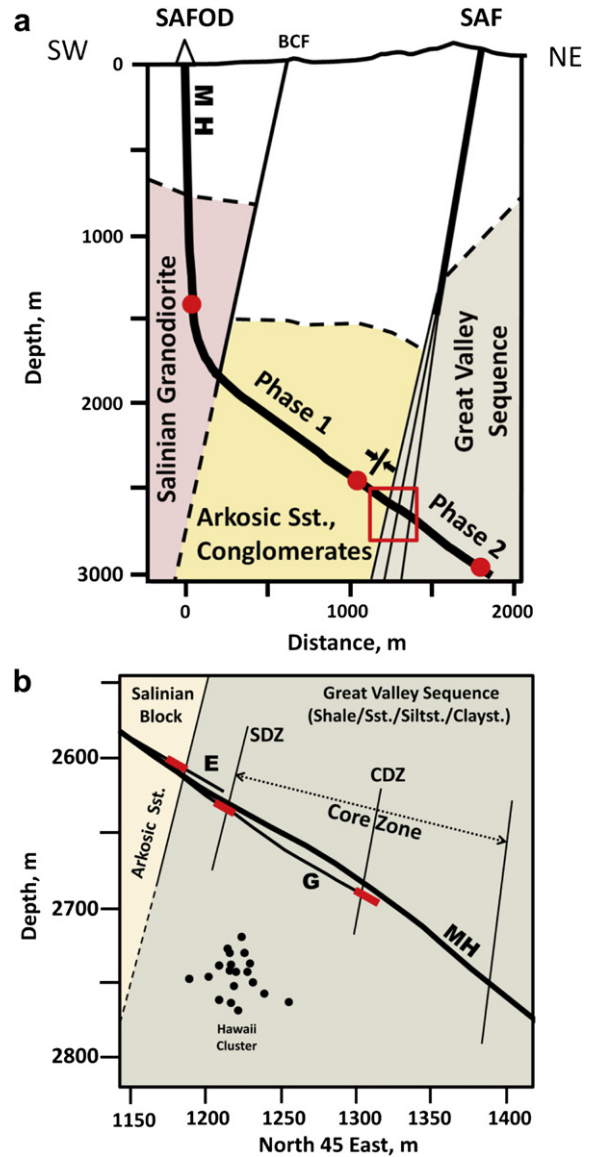


**Fig. 1.** Profile of the SAFOD drill holes marked with location of core intervals. (a) SAFOD main hole (MH) with location of Phase 1 and Phase 2 spot core intervals (solid red circles). Lithological units SW of SAF are collectively known as the Salinian Block. (b) Enlarged inset box showing Salinian–Great Valley Formation contact and position of the Phase 3 lateral holes E and G with respect to MH. Coring intervals in lateral holes are shown with solid red rectangles. Approximate trace of the well-casing deformation zones, SDZ and CDZ, and position of SAF core zone are shown. Note that well-casing deformation was only detected in the main hole. Hawaii cluster refers to one of the two target microseismicity clusters near the SAFOD boreholes. (For interpretation of the references to color in this figure legend, the reader is referred to the web version of this article.)

weaker crystallographic preferred orientation (CPO) fabric relative to the fabrics found in shale from North Sea sedimentary basin, and schist from metamorphic rocks in the Alps (also see Haines et al., 2009). Weak fault gouge CPO fabrics were attributed to randomization by heterogeneous deformation, as well as dissolution–precipitation reactions. A study by Schleicher et al. (2009) indicated that mineralogical transformation in the SAFOD damage zone and active shear zones are mainly due to pressure solution and diagenetic processes. Gratier et al. (2011) suggested that creep accommodated by pressure solution could explain the weakness of the SAF at depths greater than a few km.

Based on stress measurements in the SAFOD pilot hole, Chéry et al. (2004) argued that only a fault model with  $\mu < 0.1$  could match both the far field and the pilot hole stress data. Based on frictional sliding experiments on reconstituted gouge (lacking in-situ fabric) at room temperature, Tembe et al. (2006) reported  $\mu = 0.4$  to  $\mu = 0.55$  for bulk samples of the SAFOD clay gouge and its mostly siltstone-shale protolith. Velocity-stepping sliding experiments by Lockner et al. (2011) gave  $\mu = 0.19$  and  $\mu = 0.16$  respectively for the SDZ and CDZ core material, and showed that the material is velocity strengthening. Extrapolating from the slowest sliding rates in the experiments to the SAF creep rate of  $\leq 34$  mm/year, Lockner et al. (2011) suggested that the actual friction in the active shear zones may be as low as  $\mu = 0.16$  for SDZ and  $\mu = 0.14$  for CDZ. Carpenter et al. (2011) reported velocity-stepping sliding experiments that provided similar strength results for the SAFOD gouge as well as showing zero frictional-contact healing rates for the active shear zone materials. These results and work by others (Wintsch et al., 1995; Moore and Lockner, 2008; Tembe et al., 2009; Ikari et al., 2009; Janssen et al., 2010) suggested that friction coefficients as low as 0.1 should be expected if slip surfaces were to be lined with small amounts of weak phases such as talc or amorphous material. Furthermore, friction strengths lower than those found by sliding experiments should be expected due to microstructural control of gouge strength. For example, Chester and Chester (1998), Jefferies et al. (2006), Tembe et al. (2010), and Niemeijer et al. (2010) argued that development of foliation due to accumulation of weak alteration products, especially phyllosilicates, is often associated with long-term weakening of mature crustal-scale fault zones. Foliation itself as a microstructural weakening mechanism

was investigated by Collettini et al. (2009) in an experimental study that showed intact foliated gouge samples had a lower frictional strength than their powdered equivalents. In view of the previous work described, this study is mainly focused on providing a better understanding of the microstructurally recognizable deformation mechanisms in the SAFOD samples, particularly in the active shear zones. In this respect, an important question centers on the strength implications of shear localization and whether this could be interpreted from microstructures and materials of the studied rocks.

## 2. The core samples and sections

The SAFOD main hole profile marked with spot core intervals in the phase 1 and 2 drilling and a close-up of the lateral holes E and G core intervals from the phase 3 drilling are shown in Fig. 1. The lithological unit boundaries encountered in the SAFOD main hole together with the velocity and resistivity logs are shown in Fig. 2a. A close-up of the main hole interval that includes the SAF core zone (main damage zone in Zoback et al., 2011) and location of the studied samples are shown in Fig. 2b. The drill site structural and stratigraphic units and the lithologies encountered in the SAFOD are described elsewhere (Rymer et al., 2003; Thurber et al., 2004; Darcy et al., 2004; McPhee et al., 2004; Boness and Zoback, 2006; Bradbury et al., 2007; Zoback et al., 2011). We studied 6 samples from the phase 1 and 2 spot cores and 9 samples from the phase 3 lateral holes. The study was further expanded by using a set of 6 SAFOD-provided petrographic thin sections (SAFOD, 2010) from locations other than our phase 3 core samples. Information about

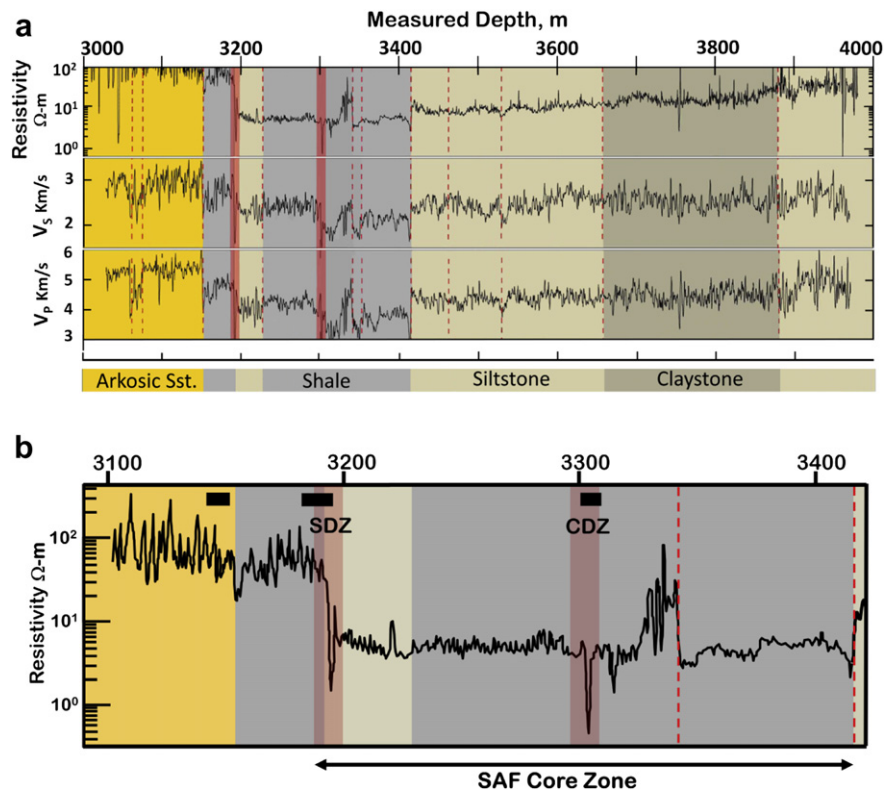


**Fig. 2.** The San Andreas Fault core zone including currently active shear zones represented by geophysical logs from the SAFOD main hole. See Jeppson et al. (2010) for additional information. (a) Changes in resistivity and seismic wave velocity within lithological units that host the fault rocks. Dashed red lines indicate minor faults or fracture zone while the two red bands are intervals of well-casing deformation that indicate active shearing. (b) A close-up of the 3100–3400m measured depth interval including the fault core zone. The entire core zone including well-casing deformation zones, SDZ and CDZ, are coincident with notable drops in resistivity. Depth range of samples used in this study (see Table 1) is marked by solid black rectangles. (For interpretation of the references to color in this figure legend, the reader is referred to the web version of this article.)

**Table 1**

The studied samples listed in order of measured depth (MD) in SAFOD boreholes. The relevant lithological and structural boundaries are marked. The depths for core sections G12–G54 (Phase 3 lateral holes) are Main Hole equivalent measured depths. Abbreviations: Box = Spot core repository box number; E and G are lateral borehole designations. For example, G25 stands for hole G, Run 2, Section 5; SAFOD TS = Petrographic thin sections provided by the SAFOD; SDZ = Southwestern Casing-Deformation Zone; CDZ = Central Casing-Deformation Zone.

Core Section	Main Hole MD, m	Studied Sample		
Box 14	3059.28	3A1	Salinian Block →	
Box 16	3061.75	5B1		
Box 17	3062.63	P3-01		
E11	3141.78	1C-2		
E13	3143.55	5A-1		
E25	3152.24	SAFOD TS		
~3174m MD				← Great valley
G12	3183.03	SAFOD TS		
G14	3184.70	SAFOD TS		
G21	3186.04	SAFOD TS		
G21	3186.53	B1XY		
G24	3188.97	7B2XY and 7B4XY	← Great valley	
G25	3189.94	A1		
G27	3191.41	SAFOD TS		
G28	3192.17	G28-01		
G31	3193.67	SM-1		
G42	3300.00	10B-1		
G43	3301.04	SAFOD TS		
G54	3308.78	G54-A1		
Box 1	3990.32	P4		
Box 2	3991.45	P5		
Box 3	3993.08	P6		

all 21 individual samples and petrographic thin sections is provided in Table 1. The set of SAFOD-provided petrographic thin sections (see SAFOD TS in Table 1) was also used in the study by Holdsworth et al. (2011). Since Table 1 provides cross-referenced sample information, here we refer to our samples by their core section designation (e.g. G25, E11).

The SDZ and CDZ active shear zone intervals are centered at 3192 m MD (~1.6 m wide) and 3302 m MD (~2.6 m wide). For technical reasons an accurate measurement of the rate of the casing deformation has not been possible except that deformation appears to be more intense in the CDZ than in the SDZ, and the deformation in each case involves some sympathetic buckling of the casing on either side of the intervals (Hickman personal communication 2010). The SAFOD geophysical logs (Fig. 2) place the CDZ and SDZ within a low-velocity zone consisting of foliated and non-foliated gouges. Our study included a thin section from G27 and a sample from G28 in the SDZ, and a thin section from G43 in the CDZ. The

sample coverage, therefore, is representative of a variety of the SAF rocks encountered during the 3 phases of drilling.

Since core samples in phase 3 were acquired by lateral drilling from the SAFOD main hole, the measured depths for hole-G samples listed in Table 1 are the main hole equivalent depths rather than the actual drilling depths in the lateral hole. The purpose of this depth conversion was to correlate the phase 3 samples with the SDZ and CDZ intervals, which were identified by borehole caliper measurements only in the main hole. Offset distances of –5.03 m and 3.96 m were applied to measured depths of the hole-G core samples. The phase 3, hole-E measured depth values were left unchanged since this run was close to the main hole and did not coincide with the casing deformation intervals. The applied correction values, provided by Zoback et al. (2011), were determined mainly by matching open-hole gamma logs (not shown in Fig. 2) from phase 2 with phase 3 logs since: 1. The SDZ and CDZ were both associated with distinct low total natural

gamma counts in the open-hole logs, and 2. Both intervals of foliated gouge in the Phase 3 core yielded distinctly low total counts in post-drilling gamma scanning. The correlation suggests that samples G27, G28 and G43 used in this study (Table 1) were probably deforming at the time of coring as part of the SDZ and CDZ.

### 3. Methods

The samples were directly cut from repository core lengths using bench saws. To prevent swelling in clay mineral phases, a CaCl<sub>2</sub> solution with slightly higher salinity than the formation fluid was used during cutting. The solution was also used for sectioning the core samples. All petrographic sections were polished sections to allow both optical and electron microscopy. The relatively less deformed samples were cut from the core billets along 3 mutually perpendicular planes without a structural or ground reference and were not impregnated prior to sectioning. The foliated gouge samples were impregnated with clear epoxy resin and cut along 2 directions perpendicular and 1 direction parallel to foliation using visual judgment. Optical transmitted and reflected light microscopy as well as high-resolution SEM was used for viewing and imaging the fault rock microstructures. Energy dispersive X-ray (EDX) with internal standards was frequently used during SEM observations for determining mineral phases and estimating the atomic wt. % of the phases. A limited number of XRF chemical composition maps were created for sample G24 to ascertain the direct relationship between foliation microstructures and mineral phase distribution. Changes in 2D image porosity across typical foliated clay gouge (sample G24 in Table 1) were estimated using digital image processing. We used digital thresholding of image pixel intensities to isolate pore spaces on binary images, from which total pore areas were measured. The measurements were made on overlapping, 1.15 mm wide tracts of backscatter SEM images over 68.7 mm total tract length. The tracts were processed one image at a time by thresholding at the narrowest and the widest possible range of pixel intensities that could represent pore areas on the image. Each step created a pair of binary images with a range of porosity values. The low-side of the range (0–10) provided the lower-bound porosity value and was considered to be the most reliable since the pixel intervals included darker tones of gray. Further details of the method may be found in Hadizadeh et al. (2010). Errors in porosity estimates due to particle plucking or filling of pores during surface preparation were assumed negligible because the gouge samples were resin impregnated. This assumption was further justified because the results were in good agreement with

the average porosity values obtained for the SAFOD gouge by porosimetry (Janssen et al., 2011). The detailed microstructural study of foliation, veins, faulting and fracturing in the samples was complemented by bulk and oriented X-ray powder diffraction (XRPD) analyses. We were primarily interested in compositional changes in a direction normal to the fault plane particularly with respect to the boundaries of the SDZ and CDZ active shear zones. A suite of 11 samples (Table 2) were selected for XRPD analysis including:

1. The fractured, but otherwise undeformed host rock (core box samples).
2. The relatively weakly deformed material such as proto-cataclasites and microbreccia (G21, G54).
3. The highly deformed material adjacent to the zones of active shear localization such as cataclasites and foliated cataclasites (G24, G25, G31).
4. Mostly foliated cataclasite and ultracataclasite gouge from the SDZ active shear zone (G28).

A total of 17 XRPD scans were carried out, 6 of which were duplicates to assure reproducibility in strongly foliated gouge materials. For bulk analyses, each sample was ground and sieved to include particles  $\leq 37 \mu\text{m}$ , packed into a sample holder and scanned at 2°/minute with a Siemens D5000Matic diffractometer at 40 kV over the range 2–61° 2 $\theta$  using Cu-K $\alpha$  radiation. The XRD scanning of sample G25 with possible presence of amorphous material was repeated 3 times, including 1 scan under the same conditions as for other runs, but using a Rigaku DMAX B diffractometer at 0.5°/minute for a more detailed scan. We found no notable difference between the three scans for sample G25. For clay phase identification, a portion of the ground samples was first washed with dilute HCl to eliminate carbonates followed by thoroughly washing and mixing the remaining mixture with distilled water. An oriented mount was made by settling the aqueous mixture onto a cellulose acetate filter and then rolling the deposited material onto a glass disk. The oriented mounts were first scanned over the range 2–30° 2 $\theta$  for all phyllosilicates and then treated with glycol and re-scanned over the range 2–22° 2 $\theta$  for smectite clays. Mineral concentrations were estimated using XRF-determined elemental compositions and the relative peak-height to peak-area on the XRPD scans. The X-ray results are shown in Table 2. The detection limit for an average mineral in these samples is ~1–3% and the analytical reproducibility was taken to be approximately equal to the square root of the amount of the phase in the analyzed powder. The XRPD scans for sample G31 from the CDZ were analyzed by Mitterpergher et al. (2011) using the Rietveld method. White light

**Table 2**

The X-ray powder diffraction results. Methods are explained in the text. See Table 1 for core section information.

N	Core section	Qtz.	Felds.	Cal.	Pyrite	Chl.	I & I-S	Verm.	Amor.	UnID
1	Box 14	39	54	0	0	0	5	0	0	2
1	Box 17	29	54	0	0	0	15	0	0	2
2	G21	62 ± 2	10	5 ± 2	2	7.5 ± 2.5	13.5 ± 1.5	0	0	0
2	G24	49 ± 1	9.5 ± 3.5	11.5 ± 0.5	1	2.5 ± 2.5	25.5 ± 0.5	0	0	1
3	G25	8.5 ± 2.5	5.5 ± 0.5	4.5 ± 0.5	0	0	36 ± 1	2.5 ± 2.5	40 ± 10	3
2	G28	10	7 ± 2	4 ± 1	0	0	0	77.5 ± 2.5	0	1.5
1	G31 <sup>a</sup>	19	25	1	1	5	49	0	0	0
2	G54	31.5 ± 0.5	19.5 ± 0.5	0	0.5 ± 0.5	29 ± 1	16.5 ± 2.5	0	0	3
1	Box 1	24	32	0	0	23	18	0	0	3
1	Box 2	22	38	0	1	24	14	0	0	1
1	Box 3	32	39	5	0	18	5	0	0	1

Abbreviations: N = number of runs; Qtz. = quartz; Felds. = Feldspars; Cal. = calcite; Chl. = chlorite; I & I-S = illite and illite-smectite; Verm. = vermiculite; Amor. = amorphous material; UnID = unidentified.

<sup>a</sup> Analysis using Rietveld method.

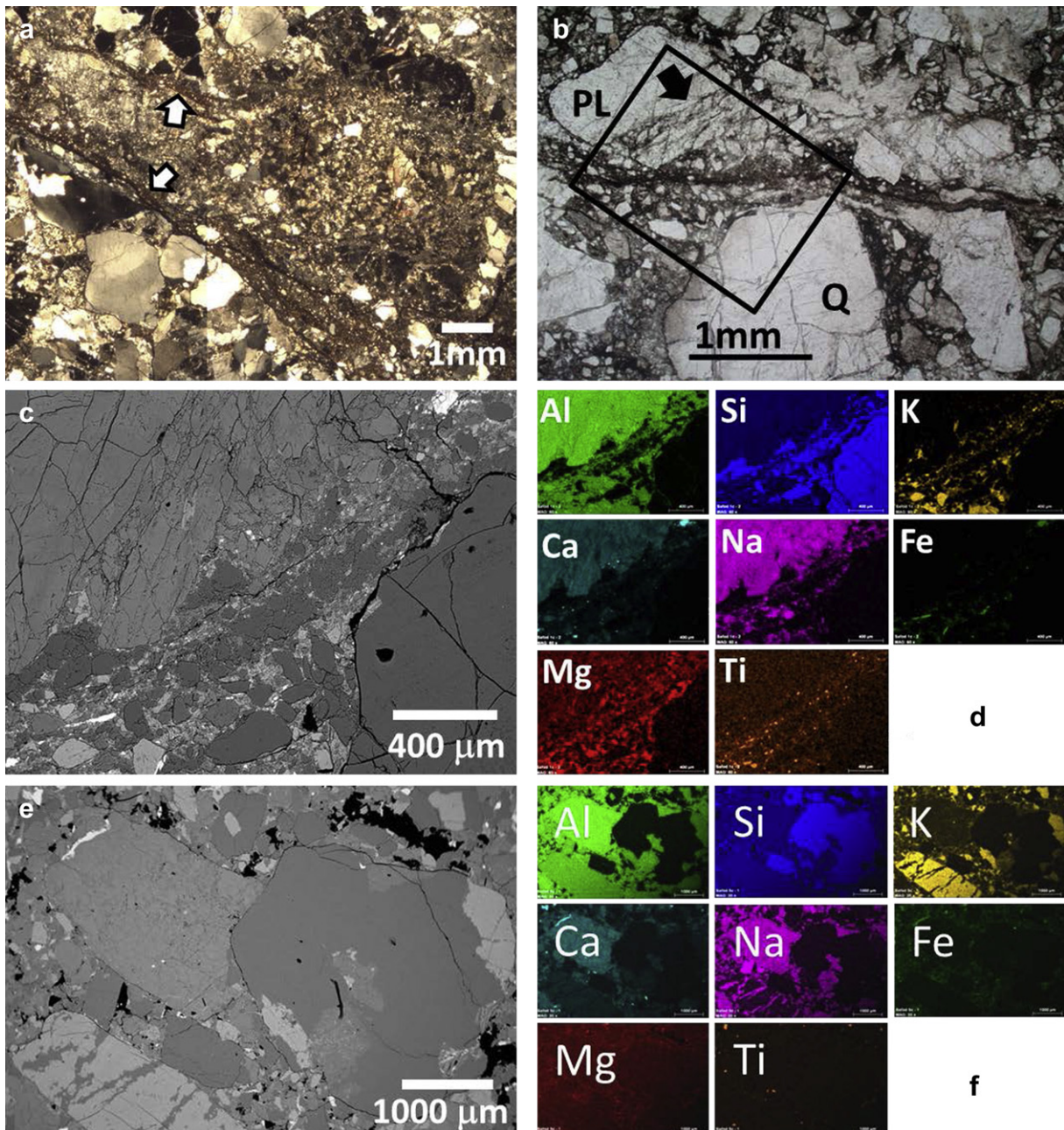


**Fig. 3.** Typical deformation microstructures outside the core zone. The data is in order of increasing measured depth toward SW border of the zone. (a) Thin gouge zone in Salinian arkosic sandstone/fine conglomerate. Highly comminuted dark streaks (arrowed) contain iron oxide and phyllosilicates. Cross polarized light (XPL) image; sample Box 16. (b) Imbricate plagioclase (PL) cleavage fractures (arrow) and grain-boundary attrition of quartz (Q) showing role of cataclasis in the development of minor gouge zones. Plane polarized light (PPL) image; sample E11. (c–d) Backscatter SEM image from inset box in b, and XRF elemental maps of the same area. The elemental maps are consistent with presence of iron oxides in the shear zone, probably passively concentrated where soluble mineral were removed by pressure solution, as well as sericitization of plagioclase feldspar. Note lack of calcite deposits and concentration of Ti in the gouge. Sample E11. (e–f) Pressure solution indentation of Na-feldspar by quartz (indenter) in coarse arkosic sandstone. The impingement area includes no calcite or clay deposits. Black spots are pore spaces. Backscatter SEM image; sample E13. (g) Indentation microfracturing and pressure solution of quartz by neighboring feldspar grain in arkosic sandstone cataclasite. Calcite crack-seal veins indicate creep opening of the indentation cracks. XPL image; sample E25. (h–i) Development of vein-cleavage fabric in shale-siltstone cataclasites of Great Valley Formation. Close-up view of calcite vein fillings transverse to dissolution contacts. XPL images; sample G12. (j) Calcite veins cross-cutting quartz-healed transgranular fractures (arrows) indicating an older deformation episode in shale-siltstone cataclasite. XPL image; sample G14. (k–l) Foliation in shale-siltstone cataclasite defined by large elongated siltstone clasts separated by clay gouge (PPL image). Inset box shows calcite-healed fractures transverse to foliation, typical of vein-cleavage fabric (XPL image). Sample G21.

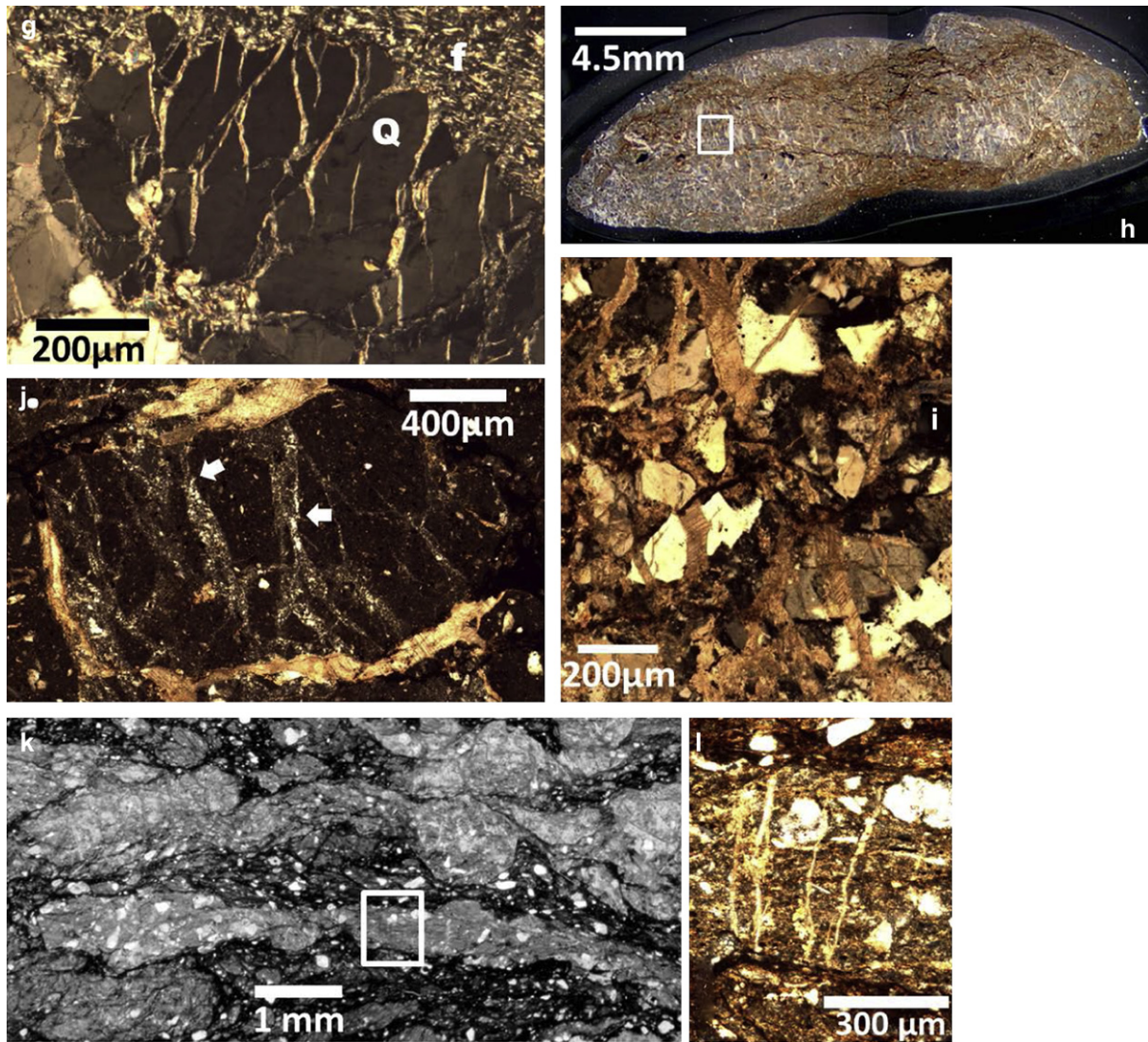


Fig. 3. (continued).

interferometry (WLI) scanning using a Zygo New View 6300 scanner was carried out on a  $\sim 4 \times 3 \times 2$  mm chip from freshly exposed striated gouge surface in sample G28. The surface sample was removed from the soft and fragile core material under microscope to avoid physical damage resembling the natural striations. The sample was mounted on glass slide using a small sticky pad and was thoroughly air-brushed before scanning.

#### 4. Microstructural and analytical observations

The SAF core zone is  $\sim 227$  m wide (3187 m–3414 m MD in the main hole) as defined by significant drops in the  $V_p$  and  $V_s$  velocity, and resistivity logs (Fig. 2b). At the scale of core sections the zone appeared to be confined to shale and mudstone units of the Great Valley sequence (Rymer et al., 2003; Thurber et al., 2004). These units are interbedded with distinct siltstone layers of up to  $\sim 5$  m thick (e.g. 3301–3306 m MD interval in Hole G). A mixed shale-siltstone gouge that probably developed close to the shale-siltstone contacts, but intervals of shale and mudstone cataclasite and siltstone cataclasite were also common

along the core sections. In addition, visible streaks and irregularly shaped serpentinite porphyroclasts of diameters up to  $\sim 0.15$  m were present in the core lengths that include SDZ and CDZ. More specific lithological description of the SAFOD core sections is provided elsewhere (see Bradbury et al., 2011; Holdsworth et al., 2011).

The deformation outside the core zone, in the Salinian arkosic sandstone, was mostly concentrated in networks of minor fault zones with mm to cm-scale apparent displacements. These features were mostly observed at distances of 126 m to 35 m from the core zone (Box 16 to E25 series, Table 1) as gouge-filled cataclastic shear zones that ranged in thickness from 1 mm to 2 cm with abundant iron oxide staining (Fig. 3a). Sliding on feldspar cleavage fractures (Fig. 3b–c) and concentration of Ti (Fig. 3d), indicating both processes of alteration and dissolution of feldspar, were frequently observed. Indentation of feldspar by quartz, with little or no local clay residual (Fig. 3e–f), and crack-seal calcite veins at the indentation sites (Fig. 3g) were also common outside and away from the core zone. Similar minor shear zones were found in the Salinian granodiorite core samples from 1464 m MD

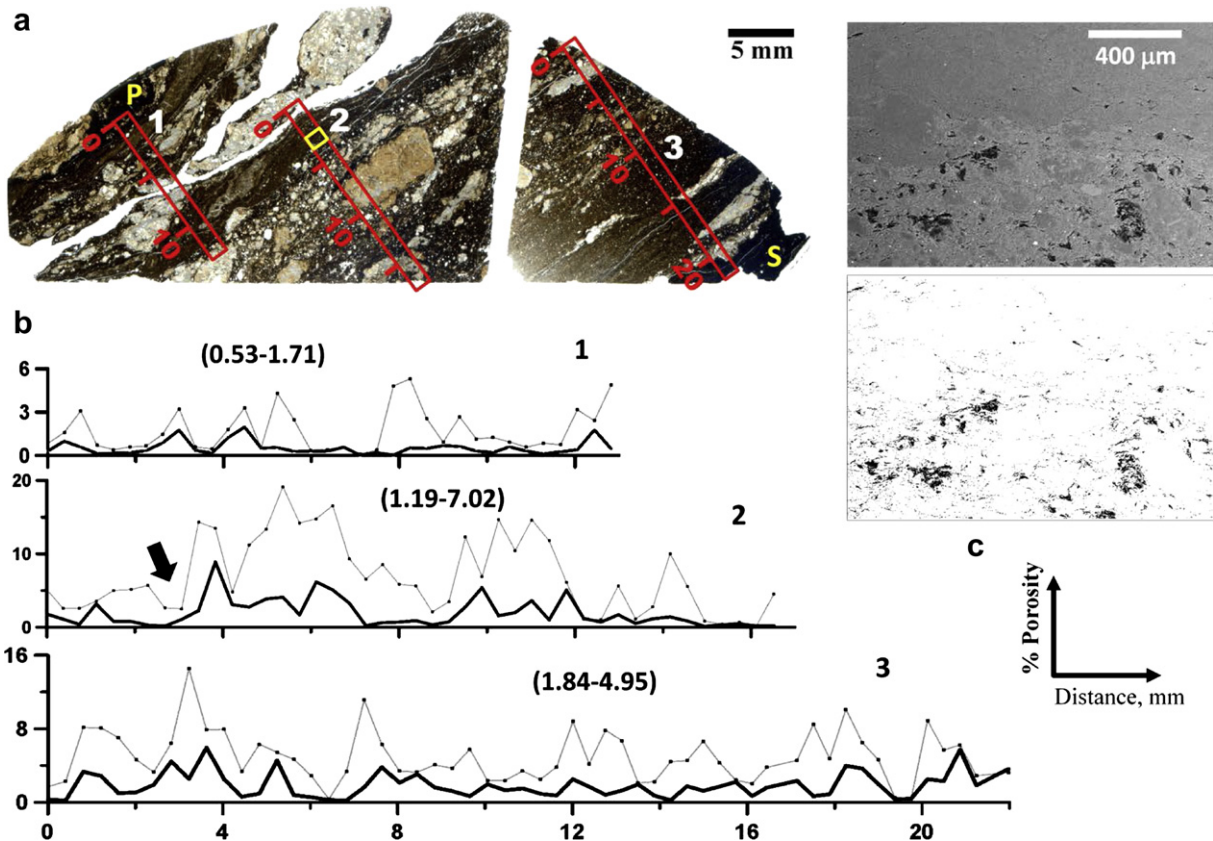


**Fig. 4.** Variations in porosity across foliation in typical shale-siltstone cataclasites of the core zone. (a) Whole section PPL image of petrographic thin sections of sample G24 showing exact position of tracts used for 2D image porosity measurement. The tracts, staggered for increased coverage, begin in host shale cataclasite P and end in deformed pyrite mass S. (b) Porosity–distance plots. Black and gray curves respectively show porosity values corresponding to narrowest (most certain) and widest (least certain) range of intensity that represented pore spaces on the images. Numbers in parenthesis are average porosity for the upper and lower-bound curves in each tract. (c) Top: backscatter SEM image located in tract 2 (inset box) showing a porosity contrast boundary in the gouge (arrow on plot 2). Bottom: binary frame based on widest pixel intensity range of pore areas on the same SEM image. Sample G24, 3188.97 m MD.

(Hadizadeh et al., 2007) and in the samples studied by Almeida et al. (2005).

The fault rocks within ~5 m of the core zone, in Great Valley shale and siltstone-shale units, were studied in thin sections from samples G12, G14, and G21. The deformation appeared more intense than in the previously described small-displacement faults mainly due to the development of foliation and greater evidence of systematic veining. Calcite veins running transverse to what appeared to be dissolution seams in the cataclasite gouge (Fig. 3h–i) indicated an early-stage cleavage development by pressure solution. There was evidence that earlier generation of transgranular fractures were sealed with quartz (Fig. 3j). A well-developed foliation in siltstone-shale cataclasites ~1 m away from the core zone border (G21) was defined by anastomosing bands of clay-rich and quartz-rich gouge (Fig. 3k). Fractures transverse to length of quartz-rich bands were sealed with calcite (Fig. 3l). The described microstructural deformation (Fig. 3a–l) was also associated with increased levels of illite-smectite phases toward the main damage zone (Table 2). Outside the core zone, the dominance of quartz-feldspar mineralogy in the SW side of the fault (Table 2) is probably due to shearing at the contact between arkosic sandstone units of the Salinian block and the Great valley shale-siltstone units.

The core zone, represented by samples G24 through G54 (Table 1), consisted of highly comminuted, altered, and foliated rocks. As described in the following, we found the microstructural

deformation to be transitional across the geophysical border of the core zone (3187 m MD). The foliation was defined by mm to sub-mm bands of clay-rich gouge intermittent with highly veined quartz-rich cataclasites (Fig. 4a). The 2-D image porosity varied across the foliation depending on clay content, distribution of hard mineral particles, and veining intensity (Fig. 4b). The porosity approached zero in quartz-rich cataclasite bands heavily veined with calcite transverse to the length of the band. The range of average porosities derived from all lower and upper bound measurements in sample G24 was 1.18–4.56%, which is comparable to the average porosity values for the SAFOD gouge obtained by porosimetry and from TEM images by Janssen et al. (2011). The foliated gouge in Fig. 5a (enlarged left side of Fig. 4a) contained microstructural evidence of reworked cataclasites as well as banding and vein fabric that appeared to be due to pressure solution. Some quartz-rich bands were vein-saturated by multiple vein network imprints. Sheared pyrite masses and feldspar alteration products in the XRF elemental maps (Fig. 5b–c) indicated hydrothermal fluid flow and mineral alterations in the gouge. The sample G42 ~1 m from the CDZ boundary revealed clear evidence of a foliation defined by pressure solution cleavage, where dissolution seams were separated by microlithons with transverse vein fabric (Fig. 5d–e). The compositional proportion of mixed-layer illite-smectite clays and other weak phases such as chlorite and vermiculite was elevated in the core zone and close to the active

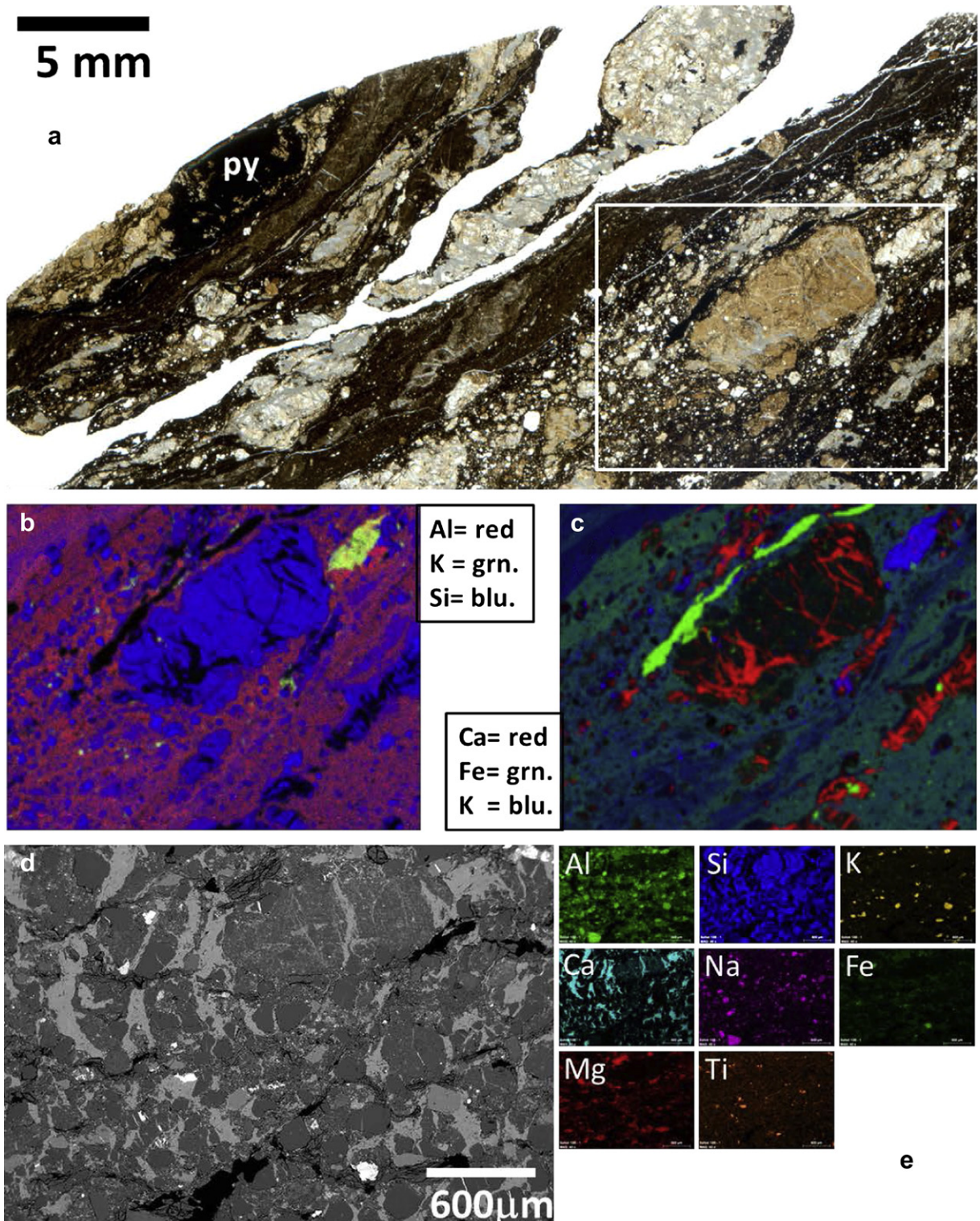


**Fig. 5.** Well-developed foliation in siltstone-shale cataclasites typical of the core zone rocks. (a) The foliation is defined by interlaced bands of siltstone-rich gouge and dark-colored clay-rich gouge. Siltstone clasts consist of variably healed cataclasites. A mass of deformed pyrite (py) forms an inverted sigma that indicates dextral sense of shear in the sample. (b) Distribution of Aluminum in XRF elemental map for inset area in the foliated gouge indicates pervasive clay mineralization. (c) XRF elemental map from the same area shows pattern of the transverse calcite veins in a quartz-rich band and reveals smearing of pyrite along foliation. Sample G24. (d) SEM backscatter image of fully-developed vein-cleavage pressure solution foliation in the core zone, ~1 m distance from the CDZ boundary. Sample G42. (e). XRF elemental maps of the area shown in d.

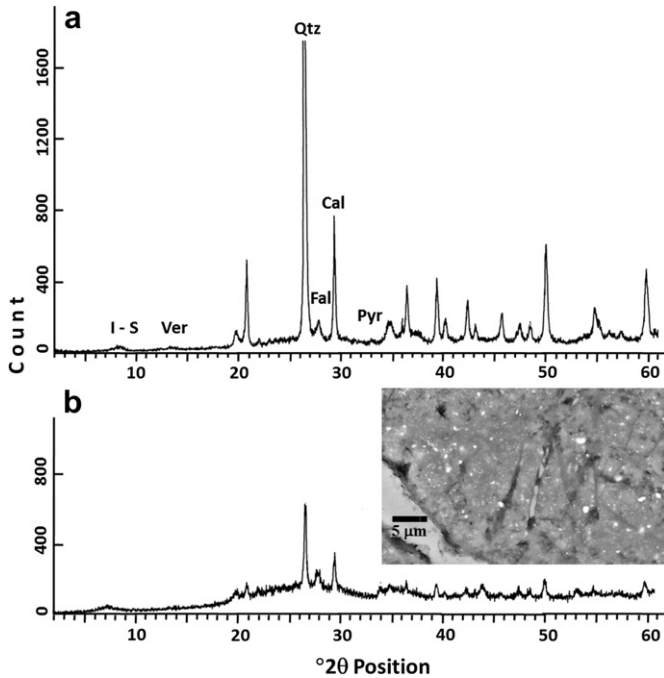


**Fig. 6.** Bulk XRPD scans comparing (a) G24 gouge sample composition from 3188.97 m MD with (b) G25 gouge sample composition from 3189.97 m MD. Raised baseline and broad peaks indicate presence of a significant component of amorphous material ~1.3 m outside active shear zone SDZ. The inset SEM image shows typical texture of the gouge. Large vein in foreground is calcite and well-distributed bright phases are pyrite particles. Note the blurred appearance of fractures in the gouge. I-S = mixed-layer illite–smectite; Ver = vermiculite; Qtz = quartz; Fal = albite feldspar; Cal = calcite; Pyr = pyrite.

shear zones (Table 2). It is reasonable to assume that the clays were derived from alteration of illite in the host shale as well as from alteration of feldspars in the gouge (see Schleicher et al., 2008). The XRPD spectra of sample G25 bordering the SDZ also indicated the presence of 30–50% of amorphous (non-crystalline) material (Table 2). The proportion of quartz and feldspar in sample G25 was anomalously low compared to other samples from the core zone, suggesting that the amorphous material was mainly composed of these two minerals. The reduced crystallinity of mineral components in sample G25 compared to those of sample G24 is demonstrated by showing the XRPD scans of these two samples side by side in Fig. 6. In close-up view, backscattered SEM images of sample G25 showed an extremely fine-grained gouge with a fuzzy texture (inset in Fig. 6b). The foliation in sample G25 was disrupted by dilation jogs and microstructures that indicate rapid volume increase of a fluid phase (Fig. 7a). In the same sample we found microstructures that appeared to be reworked dilation jogs (Fig. 7c).

The samples G27, G28 and G43 represented the SDZ and CDZ active creeping zones in this study (Table 1). The XRPD data for the SDZ sample G28 (Table 2) indicated that ~75% of the material consists of Mg-rich clay vermiculite. Although these samples were as strongly foliated as other rocks in the core zone, the XRPD, SEM-EDX, WLI and optical microscopy revealed a number of features distinct from the foliated gouge elsewhere in the core zone as follows.

1. The gouge had little or no vein network structure (Fig. 8).
2. The anastomosing phyllosilicate foliation, sigmoidal porphyroclasts, strain shadows and overgrowths (Fig. 8a–b) provided clear indication of bulk ductile flow, possibly by a combination of distributed brittle deformation, diffusive

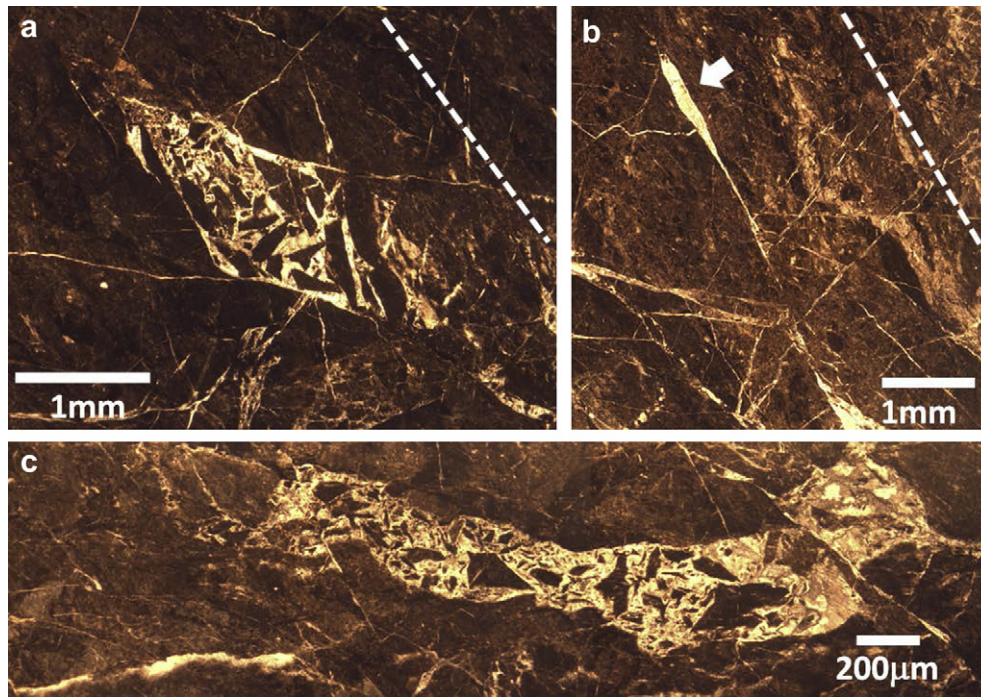


**Fig. 7.** Evidence of fluid pressures exceeding local normal stresses in the core zone, and multiple episodes of brittle fracture in foliated clay gouge ~1.2 m outside the active shear zone SDZ. Most fracture openings appear to have a shear displacement component. General trace of foliation is indicated by a dashed line. (a) Dilational jog with blocky calcite filling. Stranded angular fragments of gouge in blocky calcite matrix indicate rapid volume increase. (b) A network of cross-cutting calcite-filled microfractures is superimposed on older sheared veins. Blocky calcite vein filling in the large fracture opening (arrow) indicates an open vein crystallization environment. (c) A reworked dilation jog. PPL images from sample G25.

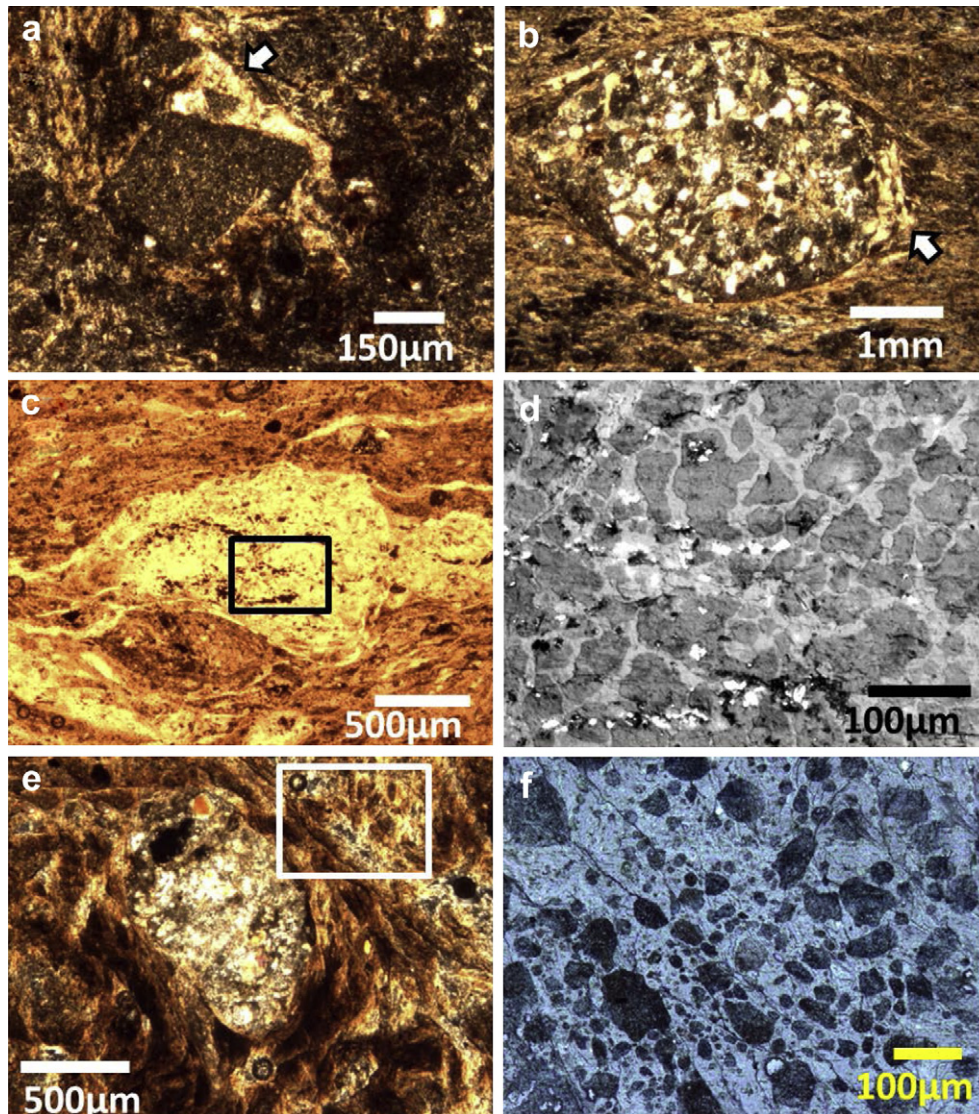


**Fig. 8.** Bulk ductile flow and alteration softening microstructures within the active shear zones. (a) Flow in clay gouge indicated by rotation of a rigid clast that has produced strain shadow (arrow) with elongated calcite crystals. (b) Sigmoid-shaped clast of arkosic sandstone cataclasite with calcite strain shadows (arrows) indicating left-lateral sense of shear in the clay gouge. (c) Optically continuous, stretched and boudinaged, serpentinite porphyroclast. (d) Enlarged view of inset box in previous image revealing nature of deformation in the porphyroclast. Alteration fragmentation of serpentinite porphyroclast is indicated by anhedral serpentinite grains in smectite-rich matrix. (e) A sub-rounded clast of arkosic sandstone cataclasite in clay gouge. (f) Enlarged view of inset box in previous image, showing smectite-rich clays mantling the cataclasite fragment. Sub-rounded quartz and feldspar grain (dark-colored) float in the clay matrix, some with concave boundaries indicative of dissolution by grain impingement. Microstructural similarity between d and f points to pervasive nature of the alteration softening in both active shear zones. Images a through d are from sample G27 (~0.2 m within SDZ); Images e and f, are from sample G43 (~1 m within CDZ). Images a, b, and e are in XPL; c is in PPL; d and f are optical reflected light images.

mass transfer, and reaction softening (see White and Knipe, 1978 for the latter mechanism). In close-up images (Fig. 8c–f), the flow microstructures were associated with matrix-supported gouge that includes quartz and feldspar with anhedral grain boundaries.

3. Locally, serpentinite porphyroclasts made approximately 5–15% of the gouge while the rest consisted of Mg-rich smectite clays, vermiculite (Table 2), or direct alteration products of the serpentinite possibly lizardite and saponite (SEM-EDX spot checks).
4. Sample G28 as well the entire G28 core section (~0.8 m) was an incohesive foliated mass. The gouge foliation was defined by sets of anastomosing P and R1 Riedel shear surfaces (Rutter et al., 1986) separating serpentinite porphyroclasts and lithic

fragments mantled by alteration products (Fig. 9a). The surfaces showed strong slickenside striations with mm to  $\mu\text{m}$ -scale spacing (Fig. 9b–d).

## 5. Discussion

We recognize three structural components of interest in the SAF near the SAFOD site: the core zone, the active shear zones (SDZ and CDZ), and features that may correspond to seismogenic asperity patch model related to the microseismic activity in the creeping segment of the SAF (see Nadeau et al., 2004; Dreger et al., 2007). The components are discussed in the above order with regard to our observations.

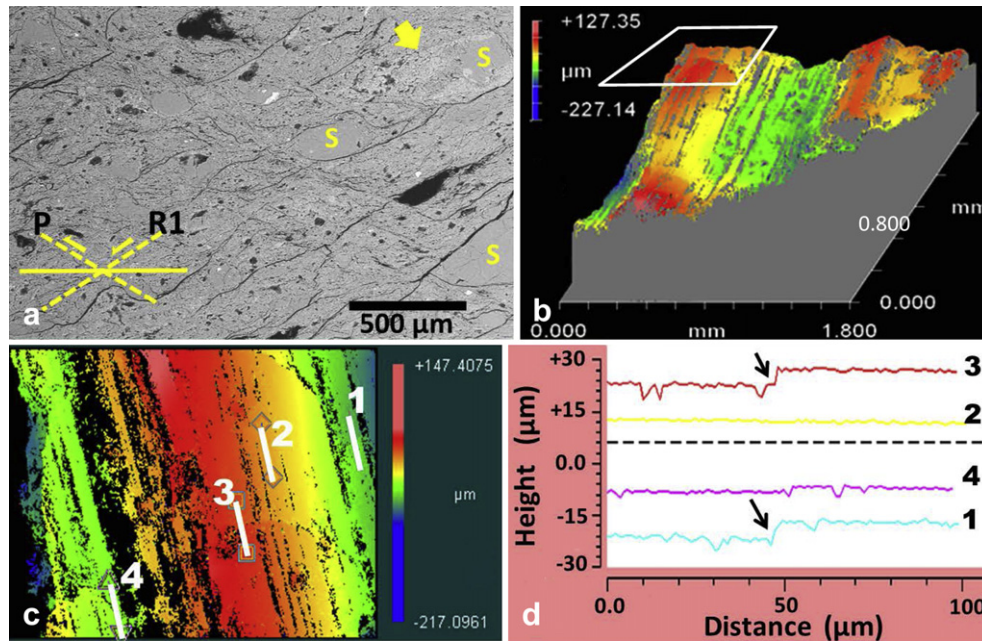


**Fig. 9.** Evidence of frictional granular flow in the active shear zones. (a) Typical lozenge-shaped microstructure of sample G28 (Sample G28 ~ 1 m within SDZ) showing microlithons separated by bands of clay-rich gouge oriented along R1 and P type Riedel shears. Clasts marked S are serpentinite porphyroclasts, some including an alteration mantle (arrow). (b) A 3-D plot of white light interferometry data revealing typical slickenside foliation surface. (c) 2-D plot of projected inset area in b showing a total relief of ~70 μm across the striations. (d) Plot of profiles 1–4 marked on c, showing slip-parallel roughness in the order of 1–3 μm. Deviations from average roughness appear to be related to hard mineral protrusions and/or microcrack steps that intersect slip surface (arrows).

### 5.1. Deformation mechanisms outside the active shear zones

The evidence presented here and supported by other SAFOD studies (Schleicher et al., 2009; Holdsworth et al., 2011; Gratier et al., 2011) show deformation in the core zone is taken place by both cataclasis and pressure solution (Fig. 3). The dominating role of pressure solution as a deformation mechanism, at least outside the active shear zones, is demonstrated by the development of a strong foliation (Fig. 5). Disruption of the foliated gouge by cataclastic deformation close to the active creeping zones (Fig. 7) is consistent with operation of both cataclasis and pressure solution mechanisms over the entire seismic cycle. The primary fault zone process that may be concluded from our observations is particle size reduction by cataclasis and widespread clay mineral authigenesis (enhanced by abundance of shale), both of which are conducive to establishment of pervasive pressure solution. Similar deformation processes were indicated in a study of fault rocks from the Median Tectonic Line in Japan (Jefferies et al., 2006). The enhancing effects on pressure solution of the presence of clay minerals have been known for sometimes (Weyl, 1959; Engelder and Marshak, 1985; Houseknecht and Hathon, 1987). Hickman and Evans (1995) suggested that clay minerals such as illite and smectite, which are capable of maintaining bound water under load, enhance pressure solution by providing higher diffusivities in the contact layer. In terms of particle size changes, Rutter (1976) showed that, where diffusion is the rate-limiting step, the rate of pressure solution creep in polycrystalline aggregates should follow an inverse cube dependence on grain size. However, if pressure solution is accompanied by mineral transformations (incongruent pressure solution), it is likely that reaction-rate is the rate-limiting step (e.g. de Meer et al., 2002; Niemeijer et al., 2009). Lack of alteration products as clay mineral residues at dissolution contacts (Fig. 3e) and presence of a cleavage-vein fabric (Fig. 5d) suggest that the pressure solution is not responsible for mineral alterations found in the studied samples and that diffusion is likely to be the rate-limiting step in the process. This interpretation is consistent

with a study of pressure solution in the same suite of SAFOD rocks by Gratier et al. (2011).

### 5.2. Deformation mechanisms in the active shear zones

In agreement with recent studies (Holdsworth et al., 2011; Jeppson et al., 2010; Zoback et al., 2011) we found that the serpentinite-bearing active shear zones SDZ and CDZ consist of intensely foliated Mg-rich phyllosilicates that unlike the surrounding core zone rocks, lack pervasive vein networks. Considering both core-scale and microstructural data, we characterize these zones as sites of large-scale shear localization within the fault core. The microstructural and compositional evidence, including clast rotation, strain shadows, streamlined flow microstructures (Fig. 8), lack of cohesion and vein networks, Riedel shears, slickenside surfaces (Fig. 9), and amorphous and weak clay phases (Table 2) are associated with the active shear zones. An abundance of phyllosilicates at the site of SDZ and CDZ has contributed to a highly developed foliation, where slip occurs on a hierarchy of surfaces in the foliated gouge, producing polished slickenside surfaces. At the finest scale, the P and R1 slip surfaces shown in Fig. 9a act as clay-lined microlithon boundaries in a wavy lozenge-shaped pattern. These observations link the shear localization by a granular flow to intrinsic (absolute) material weakness. The data suggest that shear localization is mainly by a granular flow mechanism that involves frictional sliding of microlithons set in a matrix of phyllosilicates. However, the grain-boundary sliding in this mechanism may be assisted by pressure solution, which was estimated by Gratier et al. (2011) to accommodate strain values as large as 60% by solution cleavage at the boundary of the active shear zones. Such stress-driven mass transfer in fine-grained gouge is probably efficient for distances <100 μm as might be the case in Fig. 5d–e. A similar flow mechanism was shown to operate in experimental fault gouge consisting of halite and phyllosilicates (Bos and Spiers, 2000; Niemeijer and Spiers, 2006). However, as argued for the Carboneras Fault zone (Faulkner and Lewis, 2003),

the distributed nature of the deformation and thickness of the SDZ and CDZ also are consistent with strain hardening/velocity strengthening of the weak gouge material. Lockner et al. (2011) showed that some of the weakest SAFOD gouge material ( $\mu < 0.2$ ) lies within the active shear zones. It should be noted that the stability field of smectite minerals in the active zones ( $\sim 120^\circ\text{C}$ ) is limited to about 150–200 °C. At temperature  $>200^\circ\text{C}$ , smectite clays will be replaced by Mg-Chlorites with higher friction coefficients (Frey and Robinson, 1999). To explain the creeping process at depths below the SAFOD, presence of significant proportions of stable weak phases such as talc or deformation mechanisms such as diffusive grain-boundary sliding have been invoked (Lockner et al., 2011; Holdsworth et al., 2011; Gratier et al., 2011).

### 5.2.1. The shear localization

Based on energy considerations alone, Beeler et al. (1996) argued that the strength of a fault tends to be minimized provided there is a path by which weakness can occur (also see Ben-Zion and Sammis, 2003). Amorphous material is found bordering both the SDZ (in this study) and CDZ (Janssen et al., 2010). The amorphous material reported by Janssen et al. (2010) was attributed to intense comminution, and considered to be significant as a friction reducing material in the creeping SAF. Whether the amorphous material is produced through comminution or by alteration processes, its spatial coincidence with the active shear zone is significant in terms of weakening and shear localization in the core zone. We note that further studies are needed to shed light on the genesis and distribution of the observed amorphous material. The results also suggest other weakening mechanisms that might have preceded the shear localization, including dissolution of strong load bearing minerals (quartz and feldspar) by pressure solution, and fluid assisted alteration of feldspars and serpentinite to phyllosilicates such as illite and illite-smectite clay minerals (also see Moore and Rymer, 2012). The existence of the active shear zones indicate that the weakening has occurred by a reduction in the effective (actively shearing) thickness of the fault zone rather than by widening or what may be termed a delocalization. If we let strain rate and strain ( $\tau(\dot{\gamma}, \gamma)$ ) be the only variables affecting shear strength of the fault with effective thickness  $h$ , we may rewrite equation (4) from Beeler et al. (1996) simply as  $d\tau = -1/h^2 (V\tau/\dot{\gamma} + \delta\tau/\gamma)dh$ , where  $V$  is slip velocity,  $\dot{\gamma}$  and  $\gamma$  are shear strain rate and shear strain respectively. As applied to the SAFOD site,  $dh < 0$  (shear localization condition), and the term  $V\tau/\dot{\gamma}$  is non-zero (velocity strengthening gouge). For the fault strength to be minimized through shear localization ( $d\tau/dh < 0$ ) the relative effect of displacement dependence ( $\delta\tau/\gamma$ ) must be greater than that of the velocity dependence  $V\tau/\dot{\gamma}$ , which would require a strongly displacement-weakening fault zone. A physical explanation for this mechanical behavior, as suggested by Niemeijer and Spiers (2005, 2006) experiments, is the possible role of phyllosilicates in inhibiting healing and sealing of the foliated gouge deforming by frictional granular flow assisted by stress-driven mass transfer. Lack of cohesion and vein networks in the SDZ sample support this explanation. Further support for this argument is provided by experimental results showing that the gouge material in the active shear zones is velocity strengthening (Lockner et al., 2011) and has an extremely low healing rate (Carpenter et al., 2011). It appears that the velocity strengthening gouge in the active shear zones is being sheared in the absence of pervasive restrengthening mechanisms such as cementation or fracture sealing.

### 5.3. Possible explanations for the microseismicity

The two active shear zones encountered in the drill hole are  $\sim 110$  m apart. It is reasonable to assume that the zones could vary

in width and spacing and have tendency to pinch, branch, and converge along strike. Such non-planar patterns of shear localization resulting from deformation-related lithological obstructions (material contrasts), which are likely to act as local restraining and releasing bends, have been reported from other major fault zones (e.g. Faulkner and Lewis, 2003 and Imber et al., 2008). Chester et al. (2010) noted that slip on pinched regions of the active shear zones must occur on gouge material with higher frictional strengths. The primary fault rock support for the presence of meter-scale undulations of the active shear zones is vein-sealed lenses of coarse siliciclastic cataclasites interlaced with clay gouge in the core zone (e.g. 3295 m to 3296.5 m MD, and 3301.5 m to 3303.3 m MD in Hole G). Varied-size blocks of serpentinite encountered in some drill core sections (e.g.  $\sim 0.36$  m length section at 3196.63 m MD in hole G) may serve as nucleation spots for microseismicity in the same manner described for dolomite blocks in the Carboneras fault zone (Faulkner and Lewis, 2003).

The permeability variations due to a combination of the lithological heterogeneity and fabric development are likely to affect fluid availability for alteration reactions and, therefore, the distribution of phyllosilicate phases. Field evidence and modeling (e.g. Chester and Chester, 2000; Sagy and Brodsky, 2009; Resor and Meer, 2009; Griffith et al., 2010; Mittempergher et al., 2011) suggest that the undulations of the active shear zones embedded within the core could result in non-uniform stress distribution and pore pressure build-up in the structural boundary regions. Collettini and Barchi (2002) suggested that localized, transient fluid overpressures due to presence of structural seals generate the microseismicity along the creeping Altotiberina fault zone in northern Umbria in central Italy. The distribution and geophysical estimates of the dimensions of the repeating microearthquake source suggest that regions adjacent to lithological contrasts and geometric undulations of the SAF active shear zones may act as hard patches or asperities, and should be considered as possible sources of the observed microseismicity along the SAF creeping segment.

Holdsworth et al. (2011) suggested that the core zone foliated gouge outside the active shear zones is probably inactive, but the transitional contact between the active shear zones and the surrounding core zone rocks suggests a structural coupling and raises the possibility of strain partitioning. This argument may be supported by the fabric analysis of the SAFOD foliated cataclasites that indicates fault-normal compaction in the main damage zone (Chester et al., 2010). It is possible that while most of the shear displacement is being accommodated in the CDZ and SDZ by frictional granular flow or a combination of frictional and pressure solution mechanisms, a portion of the creep is accommodated through a pressure solution-related relaxation in the core zone. If the active shear zones tend to assume an undulating (anastomosing) geometry, the pressure solution-related stress relaxation is also likely to be non-uniformly distributed. Thus an alternative explanation for the microseismicity is repetitive local healing and hardening of the fault core as it accommodates a portion of the creep rate along the SAF. Gratier et al. (2011) argued that if creeping by pressure solution results in diffusion distance  $>100\ \mu\text{m}$ , stresses do not relax and the observed microseismic activity may be attributed to local restrengthening of the gouge. The seismic rupture induces fracturing, which in turn promotes pressure solution (Gratier and Gueydan, 2007). A seismic cycle involving such fracture-and-seal processes is expected to result in episodic fluid pressure build-up. The non-uniform porosity distribution in the gouge resulting from the pressure solution cleavage development (see Fig. 4) tends to produce strike-parallel fluid barriers as well as local high fluid pressures. The disruption of foliation by episodes of higher-than-local normal stress fluid pressure was indicated by evidence of dilation jogs, reworked dilation jogs (Fig. 6), and

intrusion of shale into pre-existing veins (Mitterpergher et al., 2011; Holdsworth et al., 2011). These microstructures appeared to be confined to certain intervals of the foliated clay gouge. The occurrence of localized high fluid pressures in the main damage zone is further supported by evidence of fluid composition variations (Mitterpergher et al., 2011) and abrupt changes in real-time mud gas analysis during drilling (Wiersberg and Erzinger, 2008).

Whether the repeating microseismicity is explained by stress-releasing slip zone undulations and/or by fracture-and-seal episodes, local fluid pressures exceeding local normal stresses appears to be a mechanical requirement as seismic rupture on a hard asperity patch is likely to be prevented in a predominantly velocity strengthening fault zone (Nadeau et al., 1995; Tembe et al., 2009). An absence of higher-than-hydrostatic fluid pressures during SAFOD drilling (Zoback et al., 2011) in contrast to our microstructural evidence suggests that: 1. Intermittent high fluid pressure events must have occurred in the past, and 2. The current high fluid pressures, if any, are localized. The possible explanations for the microseismicity discussed here are consistent with the clustered and contained nature of the seismicity in the creeping segment.

## 6. Conclusions

The microstructural evidence suggests that cataclasis and pressure solution alternated in the core zone of the creeping segment of San Andreas Fault North of Parkfield, California. The pressure solution, assisted by alteration of feldspars to phyllosilicates and episodic particle size reduction by cataclasis, has been responsible for the development of the strongly foliated structure of the gouge in this segment of the fault.

The weakest material of the fault zone is found at the borders and within the currently active shear zones, suggesting that the zones represent large-scale shear localization within the SAF core zone. The energy considerations for shear localization require that the zones are strongly displacement-weakening. This theoretical requirement is consistent with a granular-type flow mechanism involving frictional sliding of the gouge microlithons along phyllosilicate-lined Riedel shear surfaces, possibly coupled with stress-driven diffusive mass transfer. The velocity strengthening weak gouge in the currently active shear zones is deforming in the absence of pervasive restrengthening mechanisms such as cementation or fracture sealing.

The study suggests two possible mechanisms for the repeating microearthquakes in the creeping fault zone. Seismic fracture occurs in frictionally strong regions (asperity patches) of the damage zone associated with stress-concentrating undulations and material contrast points. Alternatively, the asperity patches are fracture-and-seal regions in the fault core where the pressure solution accommodates a portion of the current creep movement. Evidence of local high fluid pressures presented in this study is relevant to both these explanations.

## Acknowledgments

The authors would like to thank Dan Faulkner, Bob Holdsworth, and an anonymous reviewer whose valuable comments greatly improved the manuscript. The authors would also like to thank Steve Hickman from the USGS for his valuable comments during the entire course of this research. This research was partially supported by the U.S. National Science Foundation grant NSF-EAR-0545472 to Hadizadeh, DiToro, Mair, and Babaie. DiToro and Mitterpergher were also supported by a Progetti di Eccellenza Fondazione Cassa di Risparmio di Padova e Rovigo, and by a European Research Council Starting Grant Project 205175 (USEMS). The

Grenoble team was partially supported by CNRS-INSU natural hazards program and ANR-09-JCJC-0011-1.

## References

- Almeida, R., Chester, J.S., Chester, F.M., Kirschner, D.L., Waller, T.D., Moore, D.E., 2005. Mesoscale structure and Lithology of the SAFOD phase I and II core samples. *Eos Trans. Am. Geophys. Union* 86 (52) (Abstr. T21A–0454).
- Beeler, N.M., Tullis, T.E., Weeks, J.D., 1996. Frictional behavior of large displacement experimental faults. *J. Geophys. Res.* 101, 8697–8715.
- Ben-Zion, Y., Sammis, C.G., 2003. Characterization of fault zones. *Pure Appl. Geophys.* 160, 677–715.
- Bird, P., Kong, X., 1994. Computer simulations of California tectonics confirm very low strength of major faults. *Geol. Soc. Am. Bull.* 106, 159–174.
- Boness, N.L., Zoback, M.D., 2006. A multiscale study of the mechanisms controlling shear velocity anisotropy in the San Andreas Fault Observatory at Depth. *Geophysics* 71 (4), F131–F146.
- Bos, B., Spiers, C.J., 2000. Effect of phyllosilicates on fluid-assisted healing of gouge-bearing faults. *Earth Plan. Sci. Lett.* 184, 199–210.
- Bradbury, K.K., Barton, K.C., et al., 2007. Mineralogical and textural analyses of drill cuttings from the San Andreas Fault Observatory at Depth (SAFOD) boreholes: Initial interpretations of fault zone composition and constraints on geologic models. *Geosphere* 3, 299–318.
- Bradbury, K.K., Evans, J.P., Chester, F.M., Kirschner, D.L., 2011. Lithology and internal structure of the San Andreas Fault at depth based on characterization of phase 3 whole-rock core in the San Andreas Fault Observatory at depth (SAFOD) borehole. *Earth Planet. Sci. Lett.* 310, 131–144.
- Byerlee, J., 1993. Model for episodic flow of high-pressure water in fault zones before earthquakes. *Geology* 21, 303–306.
- Carpenter, B.M., Marone, C., Saffer, D.M., 2011. Weakness of the San Andreas Fault revealed by samples from the active fault zones. *Nat. Geosci.*, 1–4. doi:10.1038/NNGEO1089. online publ.
- Chen, T., Lapusta, N., 2009. Scaling of small repeating earthquakes explained by interaction of seismic and aseismic slip in a rate and state fault model. *J. Geophys. Res.* 114, B01311.
- Chéry, J., Zoback, M.D., Hickman, S., 2004. A mechanical model of the San Andreas Fault and SAFOD Pilot Hole stress measurements. *Geophys. Res. Lett.* 31, L15S13.
- Chester, F.M., Chester, J.S., 1998. Ultracataclastic structure and friction processes of the Punchbowl fault, San Andreas system, California. *Tectonophysics* 295, 199–221.
- Chester, F.M., Chester, J.S., 2000. Stress and deformation along wavy frictional faults. *J. Geophys. Res.* 105 (B10), 23,421–23.
- Chester, J.S., Chester, F.M., Sills, D.W., Heron, B., Almeida, R.V., Guillemette, R.N., 2010. Structure of the San Andreas Fault at SAFOD. *Eos Trans. Am. Geophys. Union* 91 (52) (Abstr. T52B-03).
- Collettini, C., Barchi, M.R., 2002. A low-angle normal fault in the Umbria region (Central Italy): a mechanical model for the related microseismicity. *Tectonophysics* 359, 97–115.
- Collettini, C., Niemeijer, A., Viti, C., Marone, C., 2009. Fault zone fabric and fault weakness. *Nature* 462, 907–910.
- d'Alessio, M.A., Williams, C.F., Burgmann, R., 2006. Frictional strength heterogeneity and surface heat flow: implications for the strength of the creeping San Andreas Fault. *J. Geophys. Res.* 111, B05410.
- Darcy, K., McPhee, R.C.J., Wentworth, C.M., 2004. Crustal structure across the San Andreas Fault at the SAFOD site from potential field and geologic studies. *Geophys. Res. Lett.* 31, L12S03.
- de Meer, S., Spiers, C.J., Peach, C.J., Watanabe, T., 2002. Diffusive properties of fluid-filled grain boundaries measured electrically during active pressure solution. *Earth Plan. Sci. Lett.* 200, 147–157.
- Dreger, D., Nadeau, R.M., Chung, A., 2007. Repeating earthquake finite source models: strong asperities revealed on the San Andreas Fault. *Geophys. Res. Lett.* 34, L23302.
- Engelder, T., Marshak, S., 1985. Disjunctive cleavage formed at shallow depths in sedimentary rocks. *J. Struct. Geol.* 7, 327–343.
- Faulkner, D.R., Rutter, E.H., 2001. Can the maintenance of over pressured fluids in large strike-slip fault zones explain their apparent weakness? *Geology* 29, 503–506.
- Faulkner, D.R., Lewis, A.C., 2003. Rutter, E. H. On the internal structure and mechanics of large strike-slip fault zones: field observations of the Carboneras fault in southeastern Spain. *Tectonophysics* 367, 235–251.
- Frey, M., Robinson, D., 1999. *Low-grade Metamorphism*. Blackwell Science, Cambridge, 313 pp.
- Fulton, P.M., Saffer, D.M., 2009. Potential role of mantle-derived fluids in weakening the San Andreas Fault. *J. Geophys. Res.* 114, B07408.
- Fulton, P.M., Saffer, D.M., Bekins, B.A., 2009. A critical evaluation of crustal dehydration as the cause of an overpressured and weak San Andreas Fault. *Earth Plan. Sci. Lett.* 284, 447–454.
- Gratier, J.P., Gueydan, F., 2007. Deformation in the presence of fluids and mineral reactions: effect of fracturing and fluid-rocks interaction on seismic cycle. In: Handy, M.R., Hirth, G., Hovius, N. (Eds.), *Tectonic Faults: Agent of Change on a Dynamic Earth*. The MIT Press, Cambridge, Mass., USA, pp. 319–356.
- Gratier, J.-P., Richard, J., Renard, F., Mitterpergher, S., Doan, M.-L., Di Toro, G., Hadizadeh, J., Boullier, A.-M., 2011. Aseismic sliding of active faults by pressure

- solution creep: evidence from the San Andreas Fault Observatory at Depth. *Geology* 39, 1131–1134.
- Griffith, W.A., Nielsen, S., Di Toro, G., Smith, S.A.F., 2010. Rough faults, distributed weakening, and off-fault deformation. *J. Geophys. Res.* 115, B08409.
- Hadizadeh, J., Babaie, H. A., DiToro, G., Mair, K., 2007. What is the role of minor gouge zones in the damage zone of the SAF system? Proceedings 3rd Annual Earth Scope National Meeting, Monterey, CA.
- Hadizadeh, J., Sehhati, R., Tullis, T.E., 2010. Porosity and particle shape changes leading to shear localization in small-displacement faults. *J. Struct. Geol.* 32, 1712–1720.
- Haines, S.H., van der Pluijm, B.A., Ikari, M.J., Saffer, D.J., Marone, C., 2009. Clay fabrics in natural and artificial gouge. *J. Geophys. Res.* 114, B05406.
- Hickman, S.H., Evans, B., 1995. Kinetics of pressure solution at halite-silica interfaces and intergranular clay film. *J. Geophys. Res.* 100, 13113–13132.
- Hickman, S., Zoback, M.D., 2004. Stress orientations and magnitudes in the SAFOD Pilot Hole. *Geophys. Res. Lett.* 31, L15512.
- Holdsworth, R.E., van Diggelen, E.W., Spiers, C.J., de Bresser, H., Walker, R.J., Bowen, L., 2011. Fault rocks from the SAFOD core samples: implications for weakening at shallow depths along the San Andreas Fault. *California. J. Struct. Geol.* 33, 132–144.
- Houseknecht, D.W., Hathon, L.A., 1987. Petrographic constraints on models of intergranular pressures solution in quartzose sandstones. *Appl. Geochem.* 2, 507–521.
- Ikari, M.J., Saffer, D.M., Marone, C., 2009. Frictional and hydrologic properties of clay-rich fault gouge. *J. Geophys. Res.* 114, B05409.
- Imanishi, K., Ellsworth, W.L., 2006. Source scaling relationships of microearthquakes at Parkfield, CA, determined using the SAFOD pilot hole seismic array. In: Abercrombie, R., et al. (Eds.), *Earthquakes: Radiated Energy and the Physics of Earthquake Faulting*. AGU Geophys. Monog. Series, 170, pp. 81–90.
- Inoue, A., Utada, M., 1991. Smectite-to-chlorite transformation in thermally metamorphosed volcanoclastic rocks in the Kamikita area, northern Honshu, Japan. *Am. Mineral.* 76, 628–640.
- Imber, J., Holdsworth, R.E., Smith, S.A.F., Jeffries, S.P., Collettini, C., 2008. Frictional-viscous flow, seismicity and the geology of weak faults: a review and future directions. *Geol. Soc. London Spec. Publ.* 299, 151–173.
- Janssen, C., Wirth, R., Rybacki, E., Naumann, R., Kemnitz, H., Wenk, H.-R., Dresen, G., 2010. Amorphous material in SAFOD core samples (San Andreas Fault): evidence for crush- origin pseudotachylites? *Geophys. Res. Lett.* 37, L01303.
- Janssen, C., Wirth, R., Reinicke, A., Rybacki, E., Naumann, R., Wenk, H.-R., Dresen, G., 2011. Nanoscale porosity in SAFOD core samples (San Andreas Fault). *Earth Plan. Sci. Lett.* 301, 179–189.
- Jeffries, S.P., Holdsworth, R.E., Shimamoto, T., Takagi, H., Lloyd, G.E., Spiers, C.J., 2006. Origin and mechanical significance of foliated cataclastic rocks in the cores of crustal- scale faults: Examples from the Median Tectonic Line, Japan. *J. Geophys. Res.* 111, B12303.
- Jeppson, T.N., Bradbury, K.K., Evans, J.P., 2010. Geophysical properties within the San Andreas Fault zone at the San Andreas Fault observatory at depth and their relationships to rock properties and fault zone structure. *J. Geophys. Res.* 115, B12423.
- Lachenbruch, A., Sass, J., 1992. Heat flow from Cajon Pass, fault strength, and tectonic implications. *J. Geophys. Res.* 97, 4995–5015.
- Lockner, D.A., Morrow, C., Moore, D., Hickman, S., 2011. Low strength of deep San Andreas Fault gouge from SAFOD core. *Nature* 472, 82–85.
- McGarr, J.B., Fletcher, M., Boettcher, M., Beeler, N., Boatwright, J., 2010. Laboratory-based maximum slip rates in earthquake rupture zones and radiated energy. *Bull. Seism. Soc. Am.* 100 (6), 3250–3260.
- McPhee, D.K., Jachens, R.C., Wentworth, C.M., 2004. Crustal structure across the San Andreas Fault at the SAFOD site from potential field and geologic studies. *Geophys. Res. Lett.* 31, L12S03.
- Mittemperger, S., Di Toro, G., Gratier, J.-P., Hadizadeh, J., Smith, S.A., Spiers, R., 2011. Evidence of transient increases of fluid pressure in SAFOD phase III cores. *Geophys. Res. Lett.* 38, L03301.
- Moore, D.E., Rymer, M.J., 2007. Talc-bearing serpentinite and the creeping section of the San Andreas Fault. *Nature* 448, 795–797.
- Moore, D.E., Lockner, D.A., 2008. Talc friction in the temperature range 25 °C–400 °C: Relevance for fault zone weakening. *Tectonophysics* 449, 120–132.
- Moore, D.E., Rymer, M.J., 2012. Correlation of clayey gouge in a surface exposure of serpentinite in the San Andreas Fault with gouge from the San Andreas Fault Observatory at Depth (SAFOD). *J. Struct. Geol.* 38, 51–60.
- Nadeau, R.M., Foxall, W., McEvilly, T.V., 1995. Clustering and periodic recurrence of microearthquakes on the San Andreas Fault at Parkfield, California. *Science* 267, 503–507.
- Nadeau, R.M., Johnson, L.R., 1998. Seismological studies at Parkfield VI: moment release rates and estimates of source parameters for small repeating earthquakes. *Bull. Seism. Soc. Am.* 88, 790–814.
- Nadeau, R.M., Michelini, A., Uhrhammer, R.A., Dolenc, D., McEvilly, T.V., 2004. Detailed kinematics, structure and recurrence of micro-seismicity in the SAFOD target region. *Geophys. Res. Lett.* 31, L12S08.
- Niemeijer, A.R., Spiers, C.J., 2005. Influence of phyllosilicates on fault strength in the brittle–ductile transition: insights from rock analogue experiments. In: Bruhn, D., Burlini, L. (Eds.), *High-strain Zones: Structure and Physical Properties*. Geol. Soc. London, Special Publications, vol. 245, pp. 303–327.
- Niemeijer, A.R., Spiers, C.J., 2006. Velocity dependence of strength and healing behaviour in simulated phyllosilicate-bearing fault gouge. *Tectonophysics* 427, 231–253.
- Niemeijer, A.R., Elsworth, D., Marone, C., 2009. Significant effect of grain size distribution on compaction rates in granular aggregates. *Earth Plan. Sci.* 284, 386–391.
- Niemeijer, A.R., Marone, C., Elsworth, D., 2010. Fabric induced weakness of tectonic faults. *Geophys. Res. Lett.* 37, L03304.
- Resor, P.C., Meer, V.E., 2009. Slip heterogeneity on a corrugated fault. *Earth Plan. Sci. Lett.* 288, 483–491.
- Rice, J.R., 1992. Fault stress states, pore pressure distributions, and the weakness of the San Andreas Fault. In: Evans, B., Wong, T.-F. (Eds.), *Fault Mechanics and Transport Properties of Rock: a Festschrift in Honor of W. F. Brace*. Academic, San Diego, CA, pp. 475–503.
- Rubin, A.M., Gillard, D., et al., 1999. Streaks of microearthquakes along creeping faults. *Nature* 400, 635–641.
- Rutter, E.H., 1976. The kinetics of rock deformation by pressure solution. *Phil. Trans. R. Soc. London* 283, 203–219.
- Rutter, E.H., Maddock, R.H., Hall, S.H., White, S.H., 1986. Comparative microstructures of natural and experimentally produced clay-bearing fault gouges. *Pure Appl. Geophys.* 124, 3–30.
- Rymer, M.J., Catchings, R.D., Goldman, M.R., 2003. Structure of the San Andreas Fault zone as revealed by surface geologic mapping and high-resolution seismic profiling near Parkfield, California. *Geophys. Res. Abstr.* 5, 13523.
- SAFOD, 2010. The Core Atlas (Version 4). available from: [http://www.earthscope.org/es\\_doc/data/safod/Core%20Photo%20Atlas%20v4.pdf](http://www.earthscope.org/es_doc/data/safod/Core%20Photo%20Atlas%20v4.pdf).
- Sagy, A., Brodsky, E.E., 2009. Geometric and rheological asperities in an exposed fault zone. *J. Geophys. Res.* 114
- Schleicher, A.M., Warr, L.N., van der Pluijm, B.A., 2008. On the origin of mixed-layered clay minerals from the San Andreas Fault at 2.5–3 km vertical depth (SAFOD drill hole at Parkfield, California). *Contrib. Mineral. Petrol.* 157 (2), 173–187.
- Schleicher, A.M., Tournier, S.N., van der Pluijm, B.A., Warr, L.N., 2009. Constraints on mineralization, fluid-rock interaction, and mass transfer during faulting at 2–3 km depth from the SAFOD drill hole. *J. Geophys. Res.* 114, B04202.
- Solum, J.G., van der Pluijm, B.A., 2004. Phyllosilicate mineral assemblages of the SAFOD pilot hole and comparison with an exhumed segment of the San Andreas Fault system. *Geophys. Res. Lett.* 31, L15519.
- Solum, J.G., Hickman, S., Lockner, D.A., Moore, D.E., van der Pluijm, B.E., Schleicher, A.M., Evans, J.P., 2006. Mineralogical characterization of protolith and fault rocks from the SAFOD main hole. *Geophys. Res. Lett.* 33, L21314.
- Solum, J., Hickman, S., Lockner, D.A., Tembe, S., Evans, J.P., Draper, S.D., Barton, D.C., Kirschner, D.L., Chester, J.S., Chester, F.M., van der Pluijm, B.A., Schleicher, A.M., Moore, D.E., Morrow, C., Bradbury, K., Calvin, W.M., Wong, Teng-fong, 2007. San Andreas Fault zone mineralogy, geochemistry, and physical properties from SAFOD cuttings and core. *Sci. Drill.* (Special Issue No.1).
- Tembe, S., Lockner, D.A., Solum, J.G., Morrow, C.A., Wong, Teng-fong, Moore, D.E., 2006. Frictional strength of cuttings and core from SAFOD drill hole phases 1 and 2. *Geophys. Res. Lett.* 33, L23307.
- Tembe, S., Lockner, D.A., Wong, Teng-fong, 2009. Constraints on the stress state of the San Andreas Fault with analysis based on core and cuttings from San Andreas Fault Observatory at Depth (SAFOD) drilling phases 1 and 2. *J. Geophys. Res.* 114, B11401.
- Tembe, S., Lockner, D.A., Wong, Teng-fong, 2010. Effect of clay content and mineralogy on frictional sliding behavior of simulated gouges: binary and ternary mixtures of quartz, illite, and montmorillonite. *J. Geophys. Res.* 115, B03416.
- Thurber, C., Roecker, S., Zhang, H., Baher, S., Ellsworth, W., 2004. Fine-scale structure of the San Andreas Fault and location of the SAFOD target earthquakes. *Geophys. Res. Lett.* 31, L12S02.
- Titus, S.J., DeMets, C., Tikoff, B., 2006. Thirty-five-year creep rates for the creeping segment of the San Andreas Fault and the effects of the 2004 Parkfield earthquake: constraints from alignment arrays, continuous global positioning system, and creepmeters. *Bull. Seism. Soc. Am.* 96, S250–S268.
- Townend, J., Zoback, M.D., 2000. How faulting keeps the crust strong. *Geology* 28, 399–402.
- Townend, J., Zoback, M.D., 2004. Regional tectonic stress near the San Andreas Fault in central and southern California. *Geophys. Res. Lett.* 31, L15S11.
- Waldhauser, F., Ellsworth, W.L., et al., 2004. Streaks, multiplets, and holes: high-resolution spatiotemporal behavior of Parkfield seismicity. *Geophys. Res. Lett.* 31, L18608.
- Wenk, H.-R., Kanitpanyacharoen, W., Voltolini, M., 2010. Preferred orientation of phyllosilicates: comparison of fault gouge, shale and schist. *J. Struct. Geol.* 32, 478–489.
- Weyl, P.K., 1959. Pressure solution and the force of crystallization – a phenomenological theory. *J. Geophys. Res.* 64, 2001–2025.
- White, S.H., Knipe, R.J., 1978. Transformation and reaction enhanced ductility in rocks. *J. Geol. Soc. (London)* 135, 513–516.
- Wiersberg, T., Erzinger, J., 2008. Origin and spatial distribution of gas at seismogenic depths of the San Andreas Fault from drill-mud gas analysis. *Appl. Geochem.* 23, 1675–1690.
- Wintsch, R.P., Christoffersen, R., Kronenberg, A.K., 1995. Fluid-rock reaction weakening of fault zones. *J. Geophys. Res.* 100, 13021–13032.
- Zoback, M.D., 2000. Stress of the San Andreas Fault. *Nature* 405, 31–32.
- Zoback, M., Hickman, S., Ellsworth, W., 2011. Scientific drilling into the San Andreas Fault zone – an overview of SAFOD's first five years. *Sci. Drill.* 11, 14–28.